

# Internal kinematics of dwarf satellites of MW/M31-like galaxies in TNG50

Alberto Manuel Martínez-García,<sup>1,2\*</sup> Andrés del Pino,<sup>3</sup> Ewa L. Łokas,<sup>4</sup> Roeland P. van der Marel,<sup>5,6</sup>  
and Antonio Aparicio<sup>1,2</sup>

<sup>1</sup>*Instituto de Astrofísica de Canarias, Calle Vía Láctea S/N, E-38205 La Laguna, Tenerife, Spain*

<sup>2</sup>*Universidad de La Laguna, Dpto. Astrofísica, Avda. Astrofísico Fco. Sánchez S/N, E-38206 La Laguna, Tenerife, Spain*

<sup>3</sup>*Centro de Estudios de Física del Cosmos de Aragón (CEFCA), Unidad Asociada al CSIC, Plaza San Juan 1, 44001, Teruel, Spain*

<sup>4</sup>*Nicolaus Copernicus Astronomical Center, Polish Academy of Sciences, Bartycka 18, 00-716 Warsaw, Poland*

<sup>5</sup>*Space Telescope Science Institute, 3700 San Martin Drive, Baltimore, MD 21218, USA*

<sup>6</sup>*Center for Astrophysical Sciences, The William H. Miller III Department of Physics & Astronomy, Johns Hopkins University, Baltimore, MD 21218, USA*

Accepted 2023 September 21. Received 2023 September 20; in original form 2023 July 25

## ABSTRACT

We present a kinematic study of a thousand of dwarf satellites of MW/M31-like hosts from the IllustrisTNG50 simulation. Internal kinematics were derived for all the snapshots to obtain a historical record of their rotation velocity in the plane of the sky ( $|V_T|$ ) and the amplitude of their velocity gradients along the line of sight ( $A_{\text{grad}}^{v_z}$ ) measured from the host. For the majority of the satellites, we initially detected rotation in the plane of the sky (65%) or velocity gradients (80%), and this was progressively reduced to 45% and 68% at  $z = 0$ , respectively. We find that the evolution of the rotation in the plane of the sky and the velocity gradients differs according to type of dwarfs, which could be explained in terms of their different masses and orbital histories. We observe that interaction with the host has an impact on the evolution of the internal kinematics of the satellites. The rotation signal of the satellites is progressively reduced during pericentric passages, the first pericentre being especially disruptive for the initial kinematics. We observe temporary increases in  $A_{\text{grad}}^{v_z}$  during pericentric passage caused by tidal interaction with the host,  $A_{\text{grad}}^{v_z}$  increasing as the satellites approach their pericentre and dropping as they move away. In summary, we conclude that the presence of detectable rotation in dwarf satellites is not uncommon, and that the evolution of their internal kinematics is clearly affected by their interaction with the host.

**Key words:** galaxies: dwarf – galaxies: evolution – galaxies: kinematics and dynamics – Local Group

## 1 INTRODUCTION

Dwarf galaxies outnumber any other type of galaxy in the Universe. According to the  $\Lambda$  Cold Dark Matter ( $\Lambda$ CDM) model, dwarfs were the first galaxies to be formed and are the basic building blocks of larger galaxies, which are formed through mergers and gas accretion (White & Rees 1978; Blumenthal et al. 1984; Dekel & Silk 1986; Navarro et al. 1995). In this scenario present-day dwarfs would not yet have merged to form large structures and thus could conceal relevant information about the early Universe.

Local Group (LG) galaxies offer an exceptional opportunity to study dwarf galaxies, given their abundance and relative proximity (McConnachie 2012). Analysis of the nearest dwarfs provides detailed information about their resolved populations, thus making the LG an ideal laboratory for understanding dwarfs. Among the wide range of properties, stellar populations, and morphologies shown by

dwarf galaxies, there are two prominent sub-categories: dwarf irregular galaxies (dIrrs) and dwarf spheroidal galaxies (dSphs). dIrrs are gas-rich galaxies with recent star formation, and show coherent kinematics to some extent (Mateo 1998; McConnachie 2012; Kirby et al. 2014; Weisz et al. 2014; Putman et al. 2021). On the other hand, dSphs are essentially devoid of gas, with no recent star formation, and are dominated by random motions (Mateo 1998; McConnachie 2012; Weisz et al. 2014; Wheeler et al. 2017; Putman et al. 2021). In addition to all these properties shared between dSphs and dIrrs, their distribution in the LG is also different, dSphs being located close to the largest galaxies of the group and dIrrs in the outskirts (Mateo 1998). This suggests the presence of a transformation mechanism, which is thought to have converted gas-rich discy dwarfs (resembling present-day dIrrs) into gas-poor spheroids, owing to a combination of ram-pressure stripping, tidal stirring, and other environmental mechanisms (Mayer 2010 and references therein). These processes would remove the gas, stop the star formation, and disrupt the internal kinematics of the dwarf. However, according to this scenario, resulting

\* E-mail: ammtnez@iac.es

dSphs could retain some residual rotation (Klimentowski et al. 2009; Kazantzidis et al. 2011; Lokas et al. 2015).

The internal kinematics of dSphs remains one of their most intriguing and least-known aspects. The only way of performing kinematic analysis in dSphs is through the velocities of their individual stars. Initially, the kinematic data for dSphs were limited to catalogues of line of sight velocities ( $v_{\text{los}}$ ). In most cases no clear evidence of rotation was found in many dSphs (Kleyna et al. 2002; Wilkinson et al. 2004; Muñoz et al. 2005; Muñoz et al. 2006; Koch et al. 2007b,a; Walker et al. 2009), albeit for Carina, Fornax, Sculptor, Sextans, and Ursa Minor some hints of rotation based on line-of-sight velocity gradients were reported (Battaglia et al. 2008, 2011; Amorisco & Evans 2012; Fabrizio et al. 2016; Zhu et al. 2016; del Pino et al. 2017; Pace et al. 2020). However, the lack of reliable proper motion (PM) measurements did not allow clarification in most cases of whether these gradients were due to actual rotation or to projection on the sky of the PMs along the line of sight (Feast et al. 1961).

Data releases of the *Gaia* mission (Gaia Collaboration et al. 2016) in recent years have offered a unique opportunity to study LG satellites using the PMs of thousands of their stars. This has meant a revolution in our understanding of the LG. The presence of coherent motions in several dSphs has been reported using PMs from *Gaia*. In particular, rotation in the plane of the sky has been detected for Carina, Fornax, Sagittarius, and Sculptor, and velocity gradients along the line-of-sight (not affected by projection effects) have been reported for Carina, Draco, Fornax, Sagittarius, and Ursa Minor (del Pino et al. 2021; Martínez-García et al. 2021, 2022). This suggests that the presence of coherent motions in the internal kinematics of classical dSph satellites of the Milky Way (MW) may not be an uncommon feature. However, the sample of galaxies for which analysis of internal kinematics is feasible at present remains limited. The study of the internal kinematics of a dwarf satellite requires a sufficient number of member stars with solid measurements of the PMs and  $v_{\text{los}}$ . This significantly restricts analysis to a small number of MW satellites and does not allow us to draw strong conclusions regarding the frequency of these phenomena in the LG or elsewhere.

Simulations are an excellent tool for studying the internal kinematics of dSph satellites, as they allow us to complement and interpret observational results in ways that would not otherwise be possible. In many cases, tailor-made or zoom-in simulations were used to reproduce the evolution of a dSph as it interacts with a MW analogue or another dwarf under a wealth of scenarios and conditions (e.g. Klimentowski et al. 2009; Kazantzidis et al. 2011; Lokas et al. 2014, 2015; Ebrova & Lokas 2015; Cardona-Barrero et al. 2021). It is useful to understand how the interaction impacts the dwarf, whose parameters are more relevant in the evolution, and the final outcome of the kinematics. However, this kind of simulation reproduces the evolution for a limited number of dwarfs and scenarios. Cosmological simulations offer an alternative approach, allowing us to study the evolution of large samples of dwarfs under a variety of complex environments. Cosmological simulations have proved to be a remarkable tool in understanding the abundance (Engler et al. 2021), colours (Sales et al. 2015), and star formation of satellite galaxies (Joshi et al. 2021; Engler et al. 2022). Nevertheless, the study of their internal kinematics remains largely unexplored. Cosmological simulations can be an effective tool for analysing the internal kinematics of dwarf satellites, provided they have enough resolution in the baryonic particles and comprise large enough cosmological volumes.

In this paper, we present a kinematic study of dwarf satellites from the TNG50 run of the IllustrisTNG suite of simulations (Marinacci et al. 2018). We perform an analysis similar to that of Martínez-García et al. (2021, 2022) for the MW dSph satellites but using simulated

TNG50 data. This allows us to study the evolution of the internal kinematics of simulated satellites from an observational point of view and thus compare the results with previous observational studies. We assess the presence of coherent motions in the internal kinematics of dwarf satellites at  $z = 0$ , and study the evolution of their kinematics across time and the role of the host galaxies in the evolution of the kinematics.

This paper is organized as follows. In Section 2, we present data and methods, in Section 3 we present the results, and finally in Section 4 we summarize and present the main conclusions of this work.

## 2 DATA AND METHODS

### 2.1 Simulations

To study the internal kinematics of dwarf satellites we use the TNG50 run of the IllustrisTNG project (Marinacci et al. 2018; Naiman et al. 2018; Nelson et al. 2018; Springel et al. 2018; Pillepich et al. 2018b). The IllustrisTNG project consists of a suite of gravo-magnetohydrodynamic simulations that follow the evolution of dark matter, stellar particles, black holes, stellar winds, and gas cells between redshift  $z = 127$  and  $z = 0$ . For each run there are 100 snapshots available, ranging from from  $z \sim 20$  to  $z = 0$ . The simulations were run with the moving-mesh code AREPO (Springel 2010) and adopt cosmological parameters consistent with Planck Collaboration et al. (2016) ( $\Omega_{\Lambda,0} = 0.6911$ ,  $\Omega_{m,0} = 0.3089$ ,  $\Omega_{b,0} = 0.0486$ ,  $\sigma_8 = 0.8159$ ,  $n_s = 0.9667$ , and  $h = 0.6774$ ). As for the model for the formation and evolution of galaxies, IllustrisTNG uses an improved version of the Illustris model (full details of which can be found in Weinberger et al. 2017; Pillepich et al. 2018a).

The detection of galaxies is performed following a two-step process. First, the haloes are identified with the friends-of-friends (FoF; Davis et al. 1985) algorithm with linking length  $b = 0.2$ . Finally, subhaloes (galaxies) are detected using SUBFIND (Springel et al. 2001; Dolag et al. 2009). In order to trace the identified subhaloes between the snapshots, the merger trees are built using the SUBLINK algorithm (full description in Rodriguez-Gomez et al. 2015), which follows the baryonic content of the galaxies throughout the simulation.

For our study, we selected the TNG50-1 run (hereafter TNG50; Nelson et al. 2019b; Pillepich et al. 2019) of the IllustrisTNG suite. TNG50 is the run with the highest resolution in baryonic particles ( $8.5 \times 10^4 M_{\odot}$ ) and comprises a significant cosmological volume ( $\sim 50$  Mpc comoving box). These two features ensure that we can find a sizeable number of dwarf satellite galaxies with enough stellar particles to perform the analysis of their internal kinematics.

### 2.2 Selection of dwarf satellites

We aim to select dwarf satellites from TNG50 similar to those of the LG. In the first place, we choose host galaxies whose halo virial masses are comparable to the virial masses of the MW/M31 ( $0.7\text{--}3.0 \times 10^{12} M_{\odot}$ ) at  $z = 0$  (see Patel et al. 2017 and references therein). We then analyse their satellites, having selected those that meet a series of criteria, namely:

- The satellite has to belong to the halo of the host galaxy.
- It has to be located within the virial radius of the host at  $z = 0$ .
- Its maximum circular velocity has to be  $\leq 45 \text{ km s}^{-1}$  (Patel et al. 2018).
- Its stellar mass has to be  $\leq 10^9 M_{\odot}$  (Bullock & Boylan-Kolchin 2017).
- It has to contain at least 50 stellar particles at  $z = 0$ .

- The value of the flag 'SubhaloFlag' (Nelson et al. 2019a) has to be equal to one. This allows us to discard subhaloes detected by SUBFIND that are clumps of baryonic matter rather than galaxies of actual cosmological origin.
- The galaxy can be traced back up to at least  $z = 2$  (Joshi et al. 2021).

These criteria allow us to obtain a large sample of dwarf satellites ( $\sim 10^3$  galaxies) with enough stellar particles to study their internal kinematics. In order to analyse the internal kinematics of each class of dwarf, we aggregated them as dSphs and non-dSphs according to their observed properties in the LG (Weisz et al. 2014; Putman et al. 2021). The classification is based on the gas content and star formation histories of the galaxies (Bullock & Boylan-Kolchin 2017). We label 'dSph' for those dwarfs whose gas mass represents less than 1 per cent of their total mass at  $z = 0$ , and that completed 90 per cent of their star formation at  $z \geq 0.5$ . The remaining dwarfs are labelled 'non-dSphs' and can be a mixture of dIrrs, transition dwarfs, or dwarf ellipticals.

### 2.3 Derivation of internal kinematics

We derive the internal kinematics of the selected dwarf satellites for every snapshot of TNG50. For every halo and its corresponding satellites we use a galactocentric system whose origin is located at the centre of the host. We define the centre of a galaxy as the position of its most bound particle. From the centre of the host we observe the kinematics of the satellites. For all the stellar particles assigned to each subhalo by the SUBFIND algorithm, we derive their coordinates, PMs, and distances measured from the centre of the host. We then derive the internal kinematics of each of the satellites following a procedure analogous to that used by del Pino et al. (2021); Martínez-García et al. (2021) and Martínez-García et al. (2022). We introduce a co-moving frame centred on each satellite. The frame is fully described by van der Marel & Cioni (2001) and van der Marel et al. (2002). We refer the reader to del Pino et al. (2021); Martínez-García et al. (2021), and Martínez-García et al. (2022) for further details on the reference frame and its application to dSph satellites of the MW. In a nutshell, the 3-dimensional motion of the centre of the satellite galaxy is subtracted from its velocity field. This bulk motion of the centre is derived by taking the median of the velocity components of the stellar particles enclosed within the stellar half-mass radius of the galaxy. The individual 3D relative velocities of the stellar particles are decomposed into three orthogonal components:

$$v_{S,i} \equiv \frac{dD_i}{dt}, \quad v_{R,i} \equiv D_i \frac{d\rho_i}{dt}, \quad v_{T,i} \equiv D_i \sin \rho_i \frac{d\phi_i}{dt}, \quad (1)$$

where  $D_i$  is the distance of the  $i$ -th stellar particle to the observer (the centre of the host),  $\rho_i$  is the angular distance to the centre of the satellite, and  $\phi_i$  is the position angle (measured north to east). Consequently,  $v_{S,i}$  is the line-of-sight component of the velocity, and  $v_{R,i}$  and  $v_{T,i}$  are the radial and tangential components of the velocity in the plane of the sky with respect to the centre of the satellite. We derive three additional orthogonal velocity components referred to the centre of the satellite:  $v_{x,i}$ ,  $v_{y,i}$ ,  $v_{z,i}$ , where  $x$ -axis is antiparallel to the RA axis;  $y$ -axis is parallel to the Dec axis; and  $z$ -axis points towards the observer for a stellar particle located at the centre of the satellite. Figures 1 and 2 of van der Marel et al. (2002), and figure 2 of Martínez-García et al. (2022) provide further clarification on the velocity components and reference frame.

This procedure is applied to all the selected satellites in each of the snapshots, so we obtain a historic record of their internal kinematics.

However, in our analysis we only consider the internal kinematics of a satellite at a given snapshot if it meets certain criteria. The satellite has to contain at least 50 stellar particles in order to have a sufficient amount of data to study the internal kinematics and obtain statistically sound results. Additionally, the median value of  $v_{S,i}$  (henceforth  $V_S$ ) of its stellar particles has to be compatible with zero at  $1\sigma$  level in that particular snapshot. This implies that an optimal subtraction of the bulk motion of the centre of the satellite has been performed, and that its internal kinematics can therefore be trusted. We define the error of  $V_S$  as the standard error of the median of  $v_{S,i}$ ,  $1.253 \sigma_S / \sqrt{N_*}$ , where  $\sigma_S$  is the standard deviation of  $v_{S,i}$  and  $N_*$  is the number of stellar particles. In order to verify the validity of this error for the median, we performed multiple tests using bootstrap simulations to derive  $V_S$ . We find that the standard deviation of the median of the realizations of the simulations is similar to the assumed error of  $V_S$ . For a satellite in a certain snapshot meeting these requirements we give full consideration to the measurement of its rotation velocity in the plane of the sky and the presence of gradients in  $v_z$  in that particular snapshot.

We stress that in this study we analyse the internal kinematics of the simulated satellites from an observational point of view, i.e. as would be witnessed by an observer placed at the centre of the host galaxy. The internal kinematics of a satellite are therefore going to be observed as a combination of motions in the plane of the sky and along the line of sight. We derive the rotation velocity in the plane of the sky of a satellite (henceforth  $V_T$ ) by taking the median of the tangential component of the velocity ( $v_{T,i}$ ) of the individual stellar particles. We consider a galaxy to be rotating in the plane of the sky if  $V_T$  is not compatible with zero at the  $1\sigma$  level. The error in  $V_T$  is defined analogously to that of  $V_S$ , and the same tests with bootstrap simulations have been performed to verify the validity of the assumed error for  $V_T$ . Net positive values of  $V_T$  mean that the galaxy rotates in an anticlockwise direction in the plane of the sky.

For the detection of velocity gradients in the satellites, we fit a plane to the positions ( $x, y$ ) and the velocity component  $v_z$  of the stellar particles of each dwarf and snapshot using ordinary least-squares regression. The plane is defined as  $v_z = a_1 x + a_2 y + b$ . The amplitude of the gradient ( $A_{\text{grad}}^{v_z}$ ) is the square root of the quadratic sum of the fitting coefficients,  $\sqrt{a_1^2 + a_2^2}$ . We consider a galaxy to show a gradient in  $v_z$ , when  $A_{\text{grad}}^{v_z}$  is not compatible with zero at  $1\sigma$  level.

We performed multiple tests to assess the capability of detecting rotation in the plane of the sky and gradients in  $v_z$  in galaxies with different numbers of stellar particles and rotation velocities. We generated a mock spherical galaxy for which the position of the stellar particles was sampled from a random normal distribution centred on zero and a dispersion equal to 1 kpc. This produces a galaxy whose size is comparable to that of a dSph such as Ursa Minor (Irwin & Hatzidimitriou 1995). The galaxy rotates as a solid body around the  $z$ -axis with constant angular velocity ( $\omega$ ), the linear velocity of a particle being sampled from a normal random distribution centred on  $\omega R$ , where  $R$  is the distance of the particle to the centre of the galaxy, and the dispersion is equal to  $9.1 \text{ km s}^{-1}$  (the median velocity dispersion of the MW classical dSphs, McConnachie 2012). We measure the rotation velocity in the plane of the sky. In order to measure the amplitude of the gradient generated by the same rotation signal we then measure the gradient in  $v_x$  from the plane  $y - z$  ( $A_{\text{grad}}^{v_x}$ ). This procedure is repeated for 100 angular velocities between 0 and  $10 \text{ s}^{-1}$  in mock galaxies of 50, 100, 500, and 1000 stellar particles. In Figure 1 we show the recovered  $|V_T|$  and  $A_{\text{grad}}^{v_x}$  for the different an-

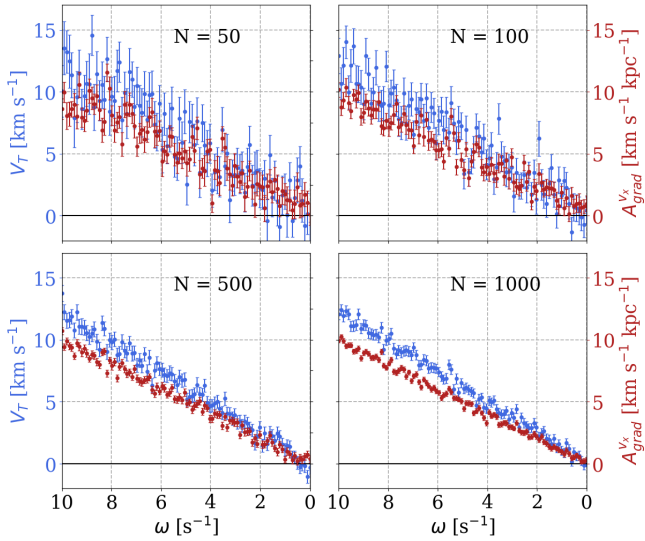


**Figure 1.** Sensitivity to the detection of rotation as rotation in the plane of the sky and as velocity gradients for galaxies with different angular velocities and numbers of stellar particles. Blue points with error bars represent the recovered rotation velocity in the plane of the sky for the mock galaxy rotating at a given angular velocity, and red points with error bars represent the recovered amplitude of the velocity gradient in  $v_x$ . The panels represent mock galaxies of 50, 100, 500, and 1000 stars. Note that we detect rotation in the plane of the sky when  $|V_T| \neq 0$  at  $1\sigma$  level and gradients in  $v_z$  when  $A_{\text{grad}}^{v_z} \neq 0$  at  $1\sigma$ .

gular velocities and numbers of stellar particles. We observe how the uncertainties are reduced with the number of stellar particles, given that they are inversely proportional to the square root of the number of stellar particles. This eases the detection of rotation in massive dwarfs. Additionally, we found that for galaxies with low angular velocities, it is easier to detect rotation as gradients rather than as rotation in the plane of the sky. This implies that the procedure to detect gradients in  $v_z$  is more sensitive to low rotation signals.

### 3 RESULTS AND DISCUSSION

#### 3.1 Dwarf satellite sample

We selected 1017 TNG50 dwarf satellites by following the criteria listed in Section 2.2. 893 were labelled dSphs and 124 non-dSphs. In Figure 2, we show the distribution of some of their properties at  $z = 0$ , namely the distance to their host ( $d_{GC}$ ), the stellar mass, the line-of-sight velocity dispersion ( $\sigma$ ), the number of pericentric passages that they have experienced during the simulation, and the look-back time of their first pericentre. Both types of dwarfs show similar distributions in  $d_{GC}$ , with non-dSphs having slightly larger values. Non-dSph galaxies generally have higher stellar masses and higher velocity dispersion. This indicates that the mass, both stellar and dynamical, of non-dSphs tends to be larger than that of dSphs. The analysis of the orbital histories reveals that dSphs have endured more pericentric passages (usually between 1 and 5) than non-dSphs (between 0 and 3), and that their first pericentric passage usually took place earlier. Therefore, dSphs are likely to have been more affected by interaction with the host.

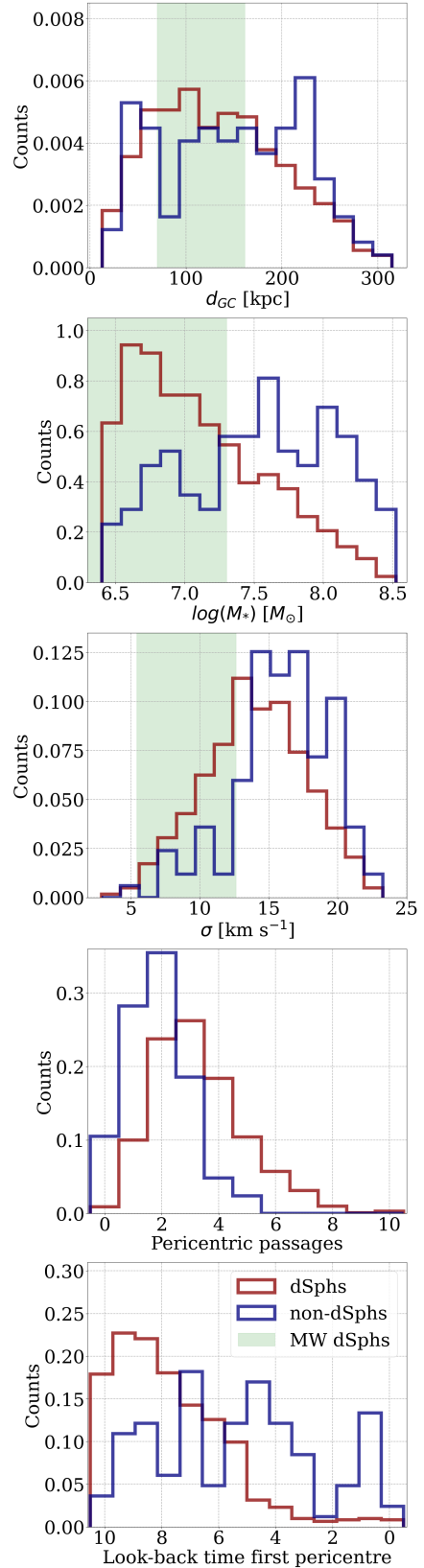


**Figure 2.** Properties of the selected dwarf satellites at  $z = 0$ . The histograms show, from top to bottom, the distribution of the galactocentric distance of the satellites to their hosts, the stellar masses, the line-of-sight velocity dispersion, the number of pericentric passages, and the look-back time of their first pericentric passage for dSphs (marked in red) and non-dSphs (marked in blue). The green-shaded areas represent the span of the corresponding properties for the classical dwarfs of the MW (McConnachie 2012).

### 3.2 Evolution of the internal kinematics

We followed the evolution of the internal kinematics of the selected satellites of TNG50 backwards from  $z = 0$ . We derived  $V_T$  and  $A_{\text{grad}}^{v_z}$  in each snapshot. Dwarfs that at a given snapshot show a poor subtraction of the motion of its centre or do not contain at least 50 stellar particles (see Section 2.3) are not considered for further study in that particular snapshot in order to preserve the quality of the analysis.

In Fig. 3, we show an example of a galaxy for which we detect rotation in the plane of the sky and a gradient in  $v_z$  at  $z = 0$ . SubhaloId = 452985 was chosen as an example given its large number of stellar particles (5518), which allows to show its kinematic patterns clearly. We show its internal kinematics in the  $x - y$  plane (i.e. in the plane of the sky, top panel) and in the  $x - z$  plane (bottom panel). We applied Voronoi tessellation (Cappellari & Copin 2003; del Pino et al. 2017) in order to increase the signal-to-noise ratio and ease the visualization of the coherent motions. The kinematic patterns can easily be seen in the corresponding panels. In the  $x - y$  plane the direction of the rotation is consistent with the calculated  $V_T$  ( $V_T = 2.5 \pm 0.3 \text{ km s}^{-1}$ ). The direction of the gradient in the figure is also consistent with the direction of the calculated gradient (PA =  $94 \pm 4$  deg; measured north to east). Note how the gradient in  $v_z$  shown in the  $x - y$  plane translates into a clear clockwise rotation pattern in the  $x - z$  plane. Velocity gradients in  $v_z$  can be caused by the rotation of the galaxy along the line of sight. Hence gradients in  $v_z$  can be considered as an indicator of the presence of rotation in perpendicular direction to the plane of the sky, as in this case, but could also be caused by tidal forces.

We detected significant rotation in the plane of the sky ( $|V_T| \neq 0$ ) and gradients in  $v_z$  ( $A_{\text{grad}}^{v_z} \neq 0$ ) in a sizeable number of systems throughout the simulation. The percentage of dwarfs for which we detect rotation in the plane of the sky and gradients in  $v_z$  does not remain constant, on the contrary, we observe a reduction with time. In Fig. 4, we show the fraction of satellites with detected rotation in the plane of the sky (top panel) and the fraction of satellites with detected gradients in  $v_z$  (bottom panel) at different look-back times/redshifts. These ratios are represented for all the galaxies (green line) and are also represented independently for dSphs (red line) and non-dSphs (blue line).

The fraction of galaxies with detected  $|V_T| \neq 0$  has clearly decreased with time, from  $\sim 65\%$  to  $45\%$  at  $z = 0$ . Initially, dSphs and non-dSphs showed similar ratios. However, those ratios started diverging around look-back time  $\sim 10$  Gyr. At  $z = 0$ , we detect rotation in the plane of the sky in  $45\%$  of dSphs and  $53\%$  of non-dSphs. The lower mass of dSphs at  $z = 0$  (Fig. 2) makes the detection of rotation in the plane of the sky more difficult than for the heavier non-dSphs, which could explain the different ratios to some extent. However, we find evidence that the difference in the ratios is more related to the different evolution of dSphs and non-dSphs than to a detection bias. We analysed the ratios of systems with  $|V_T| \neq 0$  for dSphs and non-dSphs with comparable amounts of stellar particles. We note that galaxies with comparable amounts of stellar particles have also comparable stellar masses, given that the mass of the stellar particles is roughly the same. We divided the satellites using brackets of 250 stellar particles, i.e. grouping those containing between 0 and 250 particles, between 250 and 500, and so on. We estimated the ratio of dSphs and non-dSphs with  $|V_T| \neq 0$  within each bracket and found that the ratio is generally lower for dSphs than for non-dSphs. This suggests that the overall difference in the ratios of dSphs and non-dSphs is due to an intrinsic difference in their internal kinematics. We applied the Kolmogorov-Smirnov (KS) and Anderson-Darling (AD)

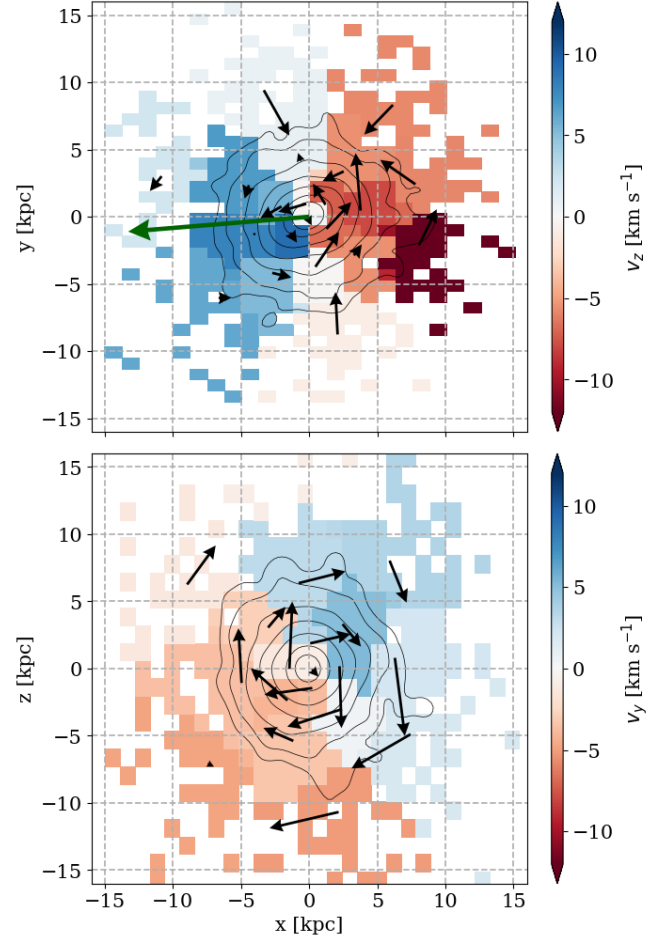


**Figure 3.** Example of a dwarf satellite (subhaloId = 452985) for which we detect rotation in the plane of the sky and a gradient in  $v_z$  at  $z = 0$ . The galaxy contains 5518 stellar particles. We applied Voronoi tessellation with cells of  $\sim 250$  particles. The top panel represents the plane  $x - y$  (i.e. the plane of the sky), the bottom panel the plane  $y - z$ . Black arrows represent the median velocity components within Voronoi cells. In order to represent the Voronoi cells and their median  $v_z$  and  $v_x$  in the planes  $x - y$  and  $y - z$ , respectively, we assign the median velocity components of each cell to all the stellar particles belonging to that particular cell. Then we bin the velocities using a rectangular grid. This significantly eases the visualization, giving a continuous appearance to the cells that is not possible to obtain representing the individual stellar particles. The colour map represents the median  $v_z$  within cells for the top panel and the median  $v_y$  for the bottom panel. The green arrow represents the direction of the gradient in  $v_z$ . The projected density of the stellar particles is shown by black contours.

tests to check the null hypothesis of samples coming from the same distribution at  $z = 0$ . We obtained p-values 0.10 and 0.04 for the KS and AD tests, respectively. Thus, the rotation velocities in the plane of the sky of dSphs and non-dSphs are unlikely to belong to the same distribution. In addition to these differences, we note that the fraction of systems with  $|V_T| \neq 0$  declines earlier and faster for dSphs than for non-dSphs, for which the ratio remains roughly constant, with a small decrease in the final snapshots of the simulation. All these differences seem to be connected to the different orbital histories and masses of dSphs and non-dSphs. The earlier decrease in the dSphs could be explained by their first pericentric passages taking place earlier (on average,  $\sim 8.5$  Gyr ago) than for non-dSphs ( $\sim 5.5$  Gyr

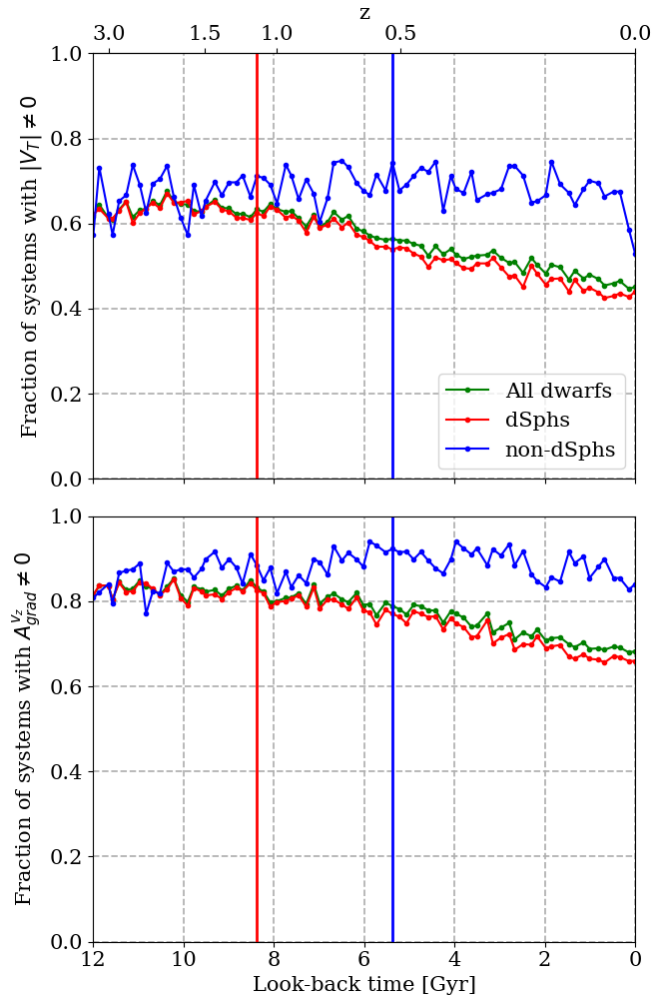


**Figure 4.** Evolution of the fraction of galaxies for which we detect rotation in the plane of sky (top panel) and velocity gradients along the line of sight (bottom panel). The green line represents the evolution of all the satellites, the red line the evolution of dSphs, and blue line the evolution of the remaining galaxies. Vertical lines mark the median look-back time for which dSphs and non-dSphs performed their first pericentric passages (colours match the corresponding type of galaxy).

ago, considering non-dSphs that do perform at least one passage). The fact that dSphs and non-dSphs initially showed similar ratios and have evolved differently depending on their orbital histories suggests that the interaction with the host plays a role in the evolution of the internal kinematics. The different final velocity distributions and the faster decrease of the fraction for dSphs are probably due to their larger number of pericentric passages and lower mass compared to non-dSphs (see Fig. 2). This leads to a more intense reduction of the rotation in the plane of the sky because of a more extensive interaction with the host in systems that are more sensitive to perturbation, owing to their lower mass.

The fraction of satellites with detected gradients in  $v_z$  has also decreased with time. Initially,  $\sim 80\%$  of satellites displayed gradients in  $v_z$  and this fraction has been reduced down to present-day 68% (with 66% for dSphs and 84% for non-dSphs). As we did for  $V_T$ , we compared the ratio of systems with gradients in  $v_z$  for dSphs and non-dSphs with similar amounts of stellar particles, finding that the ratio is always lower for dSphs. In the case of the amplitude of the

gradients at  $z = 0$ , we applied the KS and AD tests, and obtained  $p$ -values of 0.0005 and 0.001, respectively, so the distributions of the amplitude of the gradients between dSphs and non-dSphs may also be different. The fraction evolves differently depending on the category of dwarfs, similarly to what we observe for the fraction of systems rotating in the plane of the sky.

Our subsequent analysis of individual galaxies reveals that the reduction of the ratios is related to the evolution of the internal kinematics of the satellites (see Section 3.3). However, we note that other effects may also have some impact on the evolution of the ratios. The uncertainties of  $V_T$  and  $A_{\text{grad}}^{v_z}$  are inversely proportional to the square root of the number of stellar particles. As satellites orbit their host, there is a progressive mass-loss and thus a reduction in the number of stellar particles, leading to more difficult detection of  $|V_T| \neq 0$  or  $A_{\text{grad}}^{v_z} \neq 0$  at  $1\sigma$  level with time. This could explain to some extent the reduction in the ratios, yet the analysis shows that the actual reduction of the rotation signal is the main driver of this behaviour. This will be further studied in the following sections.

### 3.3 Evolution of the internal kinematics in individual satellites

We explored how  $|V_T|$  and  $A_{\text{grad}}^{v_z}$  evolve over time in individual dwarfs of our sample in order to have a more accurate picture of the impact of the interaction with the host on the internal kinematics of the satellites. In Fig. 5, we show  $|V_T|$  and  $A_{\text{grad}}^{v_z}$  at different redshifts for four satellites of TNG50. The selected examples include galaxies with a single and multiple pericentric passages and pericentric distances between  $\sim 10$  and  $\sim 50$  kpc. Their properties can be found in Table 1. We observe that initially, satellites usually have larger rotation velocities in the plane of the sky and gradients in  $v_z$  with larger amplitudes that tend to be reduced with time. As for the evolution of  $|V_T|$ , we generally observe a decrease in the average rotation velocity associated with pericentric passages. In general, the first pericentre seems to play a main role in the transformation of the rotation patterns in the plane of the sky. Tidal interaction with the host deeply distorts the original internal kinematics of the system at pericentre, removing a significant part of the rotation signal. This reduction is generally reinforced in successive passages. We observe that, in some cases, while the dwarf approaches the pericentre of its orbit there is a temporary increase of  $|V_T|$  followed by a quick drop once pericentre is reached (see e.g., `subhaloID = 428192`). However, the fact that  $|V_T|$  is measured in a perpendicular direction to the host makes it unlikely that these temporary increases are induced by tidal interaction.

The evolution of  $A_{\text{grad}}^{v_z}$  shows some similarities with  $|V_T|$ . The initially larger  $A_{\text{grad}}^{v_z}$  tends to be reduced by the successive pericentre passages.  $A_{\text{grad}}^{v_z}$  usually shows temporary increases associated with pericentric passages, i.e. it increases as dwarfs approach their pericentres and drops as they abandon them. However, unlike  $|V_T|$ , these temporary increases in  $A_{\text{grad}}^{v_z}$  are generally observed during the majority of passages. These differences in the evolution of  $|V_T|$  and  $A_{\text{grad}}^{v_z}$  are related to the way the host interacts with the satellite.  $|V_T|$  and  $A_{\text{grad}}^{v_z}$  trace the presence of rotation in a satellite from an observational point of view, from the centre of the host.  $|V_T|$  detects the presence of rotation as a 2D coherent motion in the plane of the sky and  $A_{\text{grad}}^{v_z}$  as a velocity gradient along the line of sight.  $|V_T|$  and  $A_{\text{grad}}^{v_z}$  detect the presence of rotation in a satellite in perpendicular directions. The interaction of the host with the satellite takes place in a radial direction, i.e. along the  $z$ -axis of our reference frame. Therefore, this interaction is aligned with the direction in which

**Table 1.** Properties of the selected satellites of Fig. 5. Columns: (1) subhaloID, (2) total mass, (3) stellar mass, (4) number of pericentric passages, (5) distance to the host at  $z = 0$ , (6) pericentric distance of the last pericentre, (7) look-back time of the last pericentre, (8) rotation velocity in the plane of the sky at  $z = 0$ , (9) amplitude of the gradient in  $v_z$  at  $z = 0$ , and (10) the velocity dispersion along the line of sight at  $z = 0$ .

SubhaloID	$M$ ( $10^8 M_\odot$ )	$M_*$ ( $10^6 M_\odot$ )	$n_p$	$d$ (kpc)	$d_p$ (kpc)	$t_p$ (Gyr)	$ V_T $ ( $\text{km s}^{-1}$ )	$A_{\text{grad}}^{v_z}$ ( $\text{km s}^{-1} \text{kpc}^{-1}$ )	$\sigma$ ( $\text{km s}^{-1}$ )
428192	21.3	163.9	1	61	28	4.6	$0.62 \pm 0.46$	$2.11 \pm 0.33$	19.03
554807	3.8	9.2	2	53	24	0.1	$0.06 \pm 1.10$	$2.17 \pm 0.63$	11.46
516783	4.6	8.2	3	194	24	2.5	$1.12 \pm 1.18$	$0.57 \pm 0.49$	10.33
443099	1.5	55.3	6	137	42	0.5	$0.46 \pm 0.44$	$0.43 \pm 0.50$	11.72

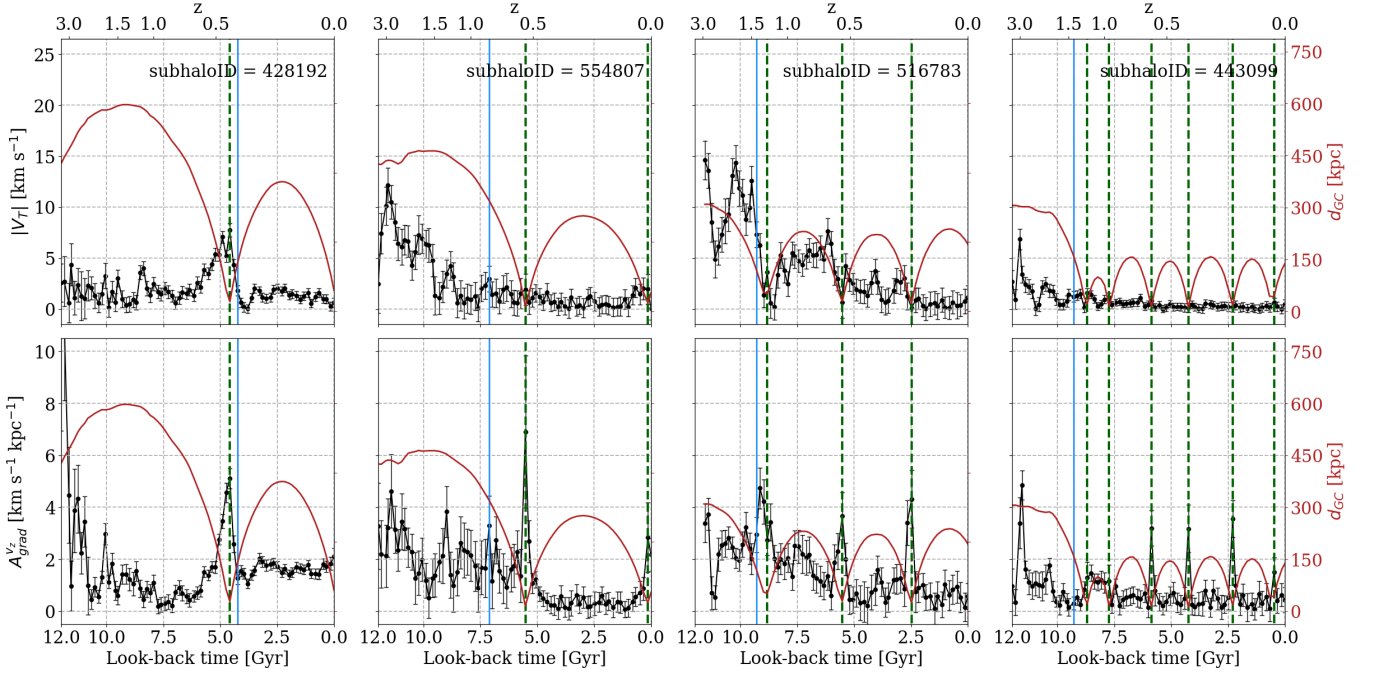


**Figure 5.** Evolution of  $|V_T|$  and  $A_{\text{grad}}^{v_z}$  for four dwarf satellites of TNG50 with pericentric distances between  $\sim 10$  and  $\sim 50$  kpc. Black lines with error bars represent  $|V_T|$  (top panels) and  $A_{\text{grad}}^{v_z}$  (bottom panels) at different look-back times/redshifts. Red solid lines represent the galactocentric distance of the satellite to the host, the pericentric passages are represented by vertical, green, dashed lines. Vertical blue lines represent the look-back time/redshift at which the satellite reached 90% of the star formation. There is clear reduction of  $|V_T|$  and  $A_{\text{grad}}^{v_z}$  associated with the pericentric passages. In the case of  $A_{\text{grad}}^{v_z}$ , we observe repeated increases when the galaxies approach the pericentres followed by sharp drops.

we measure  $A_{\text{grad}}^{v_z}$  and is perpendicular to  $|V_T|$ . This makes  $A_{\text{grad}}^{v_z}$  more sensitive to such interactions with the host. During pericentric passages, the interaction reaches its highest value. For a satellite approaching pericentre for the first time, we observe how generally  $A_{\text{grad}}^{v_z}$  increases owing to the torque induced by the tidal force. Once the galaxy abandons the pericentre, both  $|V_T|$  and  $A_{\text{grad}}^{v_z}$  decrease because their stellar content is stirred and a significant part of the rotation is removed. During successive passages, we are likely to detect temporary increases in  $A_{\text{grad}}^{v_z}$  during pericentric passages because the direction of the tidal interaction is aligned with  $v_z$ . The pericentres, however, are less likely to induce temporary increases in  $|V_T|$  given that the latter is in a direction perpendicular to the interaction and detects the presence of rotation as a 2D kinematic pattern. For both  $|V_T|$  and  $A_{\text{grad}}^{v_z}$ , we find that subsequent passages tend to reduce the rotation of the system progressively, until reaching

the low values that we detect at  $z = 0$ . In Table 2 we show the medians  $|V_T|$  and  $A_{\text{grad}}^{v_z}$  for the satellites at  $z = 0$ . This is in agreement with the progressive reduction in the ratios of systems with detected rotation in the plane of the sky and gradients in  $v_z$  (Fig. 4). The fact that interaction with the host has a different effect on  $|V_T|$  and  $A_{\text{grad}}^{v_z}$  could explain why the ratios of galaxies with  $|V_T| \neq 0$  and  $A_{\text{grad}}^{v_z} \neq 0$  evolve at slightly different rates (Fig. 4), in addition to the different sensitivity of the methods (Section 3.2). The fraction of dwarfs with  $A_{\text{grad}}^{v_z} \neq 0$  decreases more gently because  $A_{\text{grad}}^{v_z}$  tends to increase during successive pericentres. Therefore, the reduction of the fraction is slower, given that there is a continuous contribution of dwarfs that show  $A_{\text{grad}}^{v_z} \neq 0$  owing to the tidal interaction with the host.

Previous studies based on  $N$ -body simulations have analysed the evolution of the rotation in dSph satellites of MW analogues

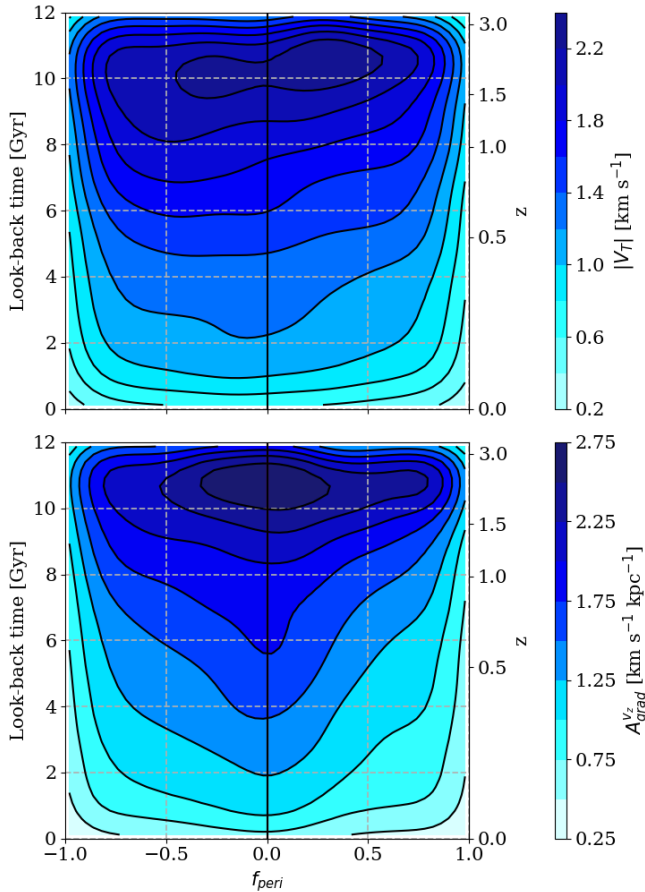


**Figure 6.** Evolution of the internal kinematics of the satellites as a function of the relative position in their orbits. The panels show  $f_{\text{peri}}$  and look-back time for all the dwarfs and snapshots. Colour-filled contours represent areas with similar  $|V_T|$  (top panel) and  $A_{\text{grad}}^{v_z}$  (bottom panel).

(Kazantzidis et al. 2011; Lokas et al. 2010, 2011, 2014, 2015), reporting similar kinds of behaviour in the evolution of their kinematics. We note that these studies follow the evolution of the rotation around the shortest principal axis of the satellites, whereas we follow it from an observational point of view, i.e. we rely on  $|V_T|$  and  $A_{\text{grad}}^{v_z}$ . They find that the rotation tends to decrease, especially at first pericentre, and that successive passages further reduce it. However, sometimes it is reported that the reduction of the rotation with the pericentres is not monotonic and may increase after a passage owing to the orientation of the system during pericentre. We also find this in the evolution of some dwarfs, as can be seen in Fig. 5 for subhaloID = 428192, where  $A_{\text{grad}}^{v_z}$  slightly increases after the first pericentre. As for the temporary increases that we detect mostly in  $A_{\text{grad}}^{v_z}$  during pericentric passages, the simulated dwarfs also show multiple examples of increases in the rotation when they approach pericentre followed by quick drop when they abandon it. We find that the evolution of the internal kinematics of the dwarf satellites of TNG50 is in good agreement with previous studies based on  $N$ -body simulations.

### 3.4 Traces of interaction with the host in the internal kinematics

In order to get a more comprehensive picture of the evolution of the internal kinematics of the dwarf satellites and the role of the interaction with the host over time, we compared simultaneously the kinematic features with the relative position of all the dwarfs in their orbits during all the snapshots of the simulation. This allows us to have a more global view of the evolution of the kinematics and to assess our findings of the previous section. The relative position of a galaxy in its orbit is given by  $f_{\text{peri}}$ , which is defined as follows:  $f_{\text{peri}} = \text{sgn}(v_R^{\text{GC}})(d_{\text{GC}} - d_p)/(d_a - d_p)$ , where  $d_{\text{GC}}$  is the distance of the satellite to the host,  $v_R^{\text{GC}}$  is the radial velocity of the satellite with respect to the host,  $d_a$  is the apocentric distance, and  $d_p$  is the pericentric distance.  $f_{\text{peri}} = 0$  means that the satellite is at the pericentre of its orbit, whereas  $|f_{\text{peri}}| = 1$  when it is at its apocentre.  $f_{\text{peri}} > 0$  implies that the galaxy is moving towards apocentre whereas  $f_{\text{peri}} < 0$  is for galaxies approaching pericentre.  $f_{\text{peri}}$  is similar to the true anomaly in Keplerian orbits and is a very useful metric, because it provides a clear idea of the position and direction of a satellite along its orbit. In Fig. 6, we represent  $f_{\text{peri}}$  and the look-back time for all the selected satellites and all the snapshots of the simulation. The data were binned and a Gaussian filter applied. Colour-filled contours encompass areas with similar  $|V_T|$  (top panel) or  $A_{\text{grad}}^{v_z}$  (bottom panel). Figure 6 allows the simultaneous study of all the dwarfs and snapshots, being a generalized version of Fig. 5, and providing additional confirmation to our findings regarding the evolution of the kinematics of individual satellites and their interaction with the host.

At first glance, we observe a clear decrease of both  $|V_T|$  and  $A_{\text{grad}}^{v_z}$  with time. Initially, the rotation velocity in the plane of the sky and the amplitude of the gradients in these systems were larger. There is a progressive reduction in both features until the low values that we currently observe at  $z = 0$  are reached. This decrease is in agreement with the reduction of the fraction of systems with detected rotation in the plane of the sky and gradients in  $v_z$  of Fig. 4 and the progressive reduction of  $|V_T|$  and  $A_{\text{grad}}^{v_z}$  with time of Figure 5. Figure 6 shows that at a given look-back time,  $|V_T|$  and  $A_{\text{grad}}^{v_z}$  tend to be systematically slightly larger in the region where  $f_{\text{peri}} < 0$ , i.e. for galaxies approaching their pericentres, compared to  $f_{\text{peri}} > 0$ , i.e. for galaxies abandoning it. This is consistent with the progressive reduction of  $|V_T|$  and  $A_{\text{grad}}^{v_z}$  associated with the pericentric passages observed in the analysis of the individual satellites. However, we observe significant differences in the evolution of  $|V_T|$  and  $A_{\text{grad}}^{v_z}$ . During the whole simulation, for a given snapshot  $A_{\text{grad}}^{v_z}$  tends to reach its highest value in the vicinity of pericentre. This is in agreement with the evolution of  $A_{\text{grad}}^{v_z}$  observed in individual satellites:  $A_{\text{grad}}^{v_z}$  tends to increase as the satellites approach their pericentre, where  $A_{\text{grad}}^{v_z}$  reaches its higher value and is then reduced as the satellites move away from pericentre. For  $|V_T|$  we find a more monotonic evolution, with a progressive reduction of  $|V_T|$  and without higher values around pericentre. This is consistent with the analysis of individual satellites from which, generally, we do not find temporary increases of  $|V_T|$  during pericentric passages. In conclusion, the different way in which  $|V_T|$  and  $A_{\text{grad}}^{v_z}$  are affected by the interaction with the host (Section 3.3) explains the different evolution of these features with time.



**Table 2.** Median  $|V_T|$ ,  $A_{\text{grad}}^{v_z}$ , and line-of-sight velocity dispersion at  $z = 0$  for the different samples of satellites galaxies. Rows: (1) Sample of satellites, (2) median  $|V_T|$  at  $z = 0$ , and (3) median  $A_{\text{grad}}^{v_z}$  at  $z = 0$ . † Median values and the interval between the 0.16 and 0.84 quantiles of the median  $|V_T|$  and  $A_{\text{grad}}^{v_z}$  of all the realizations of the MC simulation (Section 3.5). †† values taken from [McConnachie & Venn \(2020\)](#); [Martínez-García et al. \(2021, 2022\)](#).

Sample	$ V_T (z = 0)$ [ km s <sup>-1</sup> ]	$A_{\text{grad}}^{v_z}(z = 0)$ [ km s <sup>-1</sup> kpc <sup>-1</sup> ]	$\sigma$ [ km s <sup>-1</sup> ]
TNG50 satellites	0.96 ± 0.05	0.99 ± 0.04	14.23 ± 0.15
MW dSph analogues	1.08 ± 0.07	0.91 ± 0.07	10.43 ± 0.15
MW dSph analogues (MC)†	2.00 <sup>+1.72</sup> <sub>-0.90</sub>	1.45 <sup>+1.01</sup> <sub>-0.60</sub>	10.43 ± 0.15
MW dSphs††	1.86 ± 1.64	2.03 ± 0.75	9.15 ± 4.68

### 3.5 Analogues of the observed MW dSph satellites

Previous observational studies have derived  $V_T$  and  $A_{\text{grad}}^{v_z}$  for dSph satellites of the MW ([Martínez-García et al. 2021, 2022](#)). In order to compare the internal kinematics of real and simulated satellites, we further restrict our sample to match the properties of the observed dSphs. We select a subsample of TNG50 dSph satellites whose stellar mass, line-of-sight velocity dispersion, and  $M_V$  are compatible with those of Carina, Draco, Fornax, Sculptor, Sextans, and Ursa Minor ([McConnachie 2012](#)). The range of these properties is represented as shaded green areas in Fig. 2, where it can be seen that they represent the faint and low-mass end of the corresponding distributions. The resulting subsample consists of 251 dSph satellites, hereafter referred to as ‘MW dSph analogues’. The internal kinematics of the MW dSph analogues show a behaviour similar to the other simulated galaxies.

We find that the fraction of systems rotating in the plane of the sky in the subsample of MW dSph analogues was initially similar to the other simulated satellites (~65%), and decreased until reaching 39% at  $z = 0$ . This ratio is similar (45%) to that for the TNG50 dSphs at  $z = 0$ . We find similar results for the fraction of MW dSph analogues with gradients in  $v_z$ . Initially, the fraction was similar to the other TNG50 satellites (~80%) and decreased to 56% at  $z = 0$ . The ratio of MW dSph analogues with gradients in  $v_z$  at  $z = 0$  is similar (65%) to that for the TNG50 dSphs at  $z = 0$ . We observe that the behaviour in the reduction of the ratios for the full sample of TNG50 satellites and the subsample of MW dSph analogues is similar. If anything, the differences in the ratios at  $z = 0$  could be related to the lower masses of the MW dSph analogues compared to the selected satellites of TNG50. These lower masses make it more difficult to detect rotation in the plane of the sky and gradients in  $v_z$ , and also would make the MW dSph analogues more sensitive to interaction with the host so that they further reduced their rotation. The final ratios suggest that the presence of detectable rotation in satellites of MW analogues is not uncommon. For the MW satellites, the presence of rotation in the plane of the sky has been reported for Carina, Fornax, Sagittarius, and Sculptor, and gradients in  $v_z$  for Carina, Draco, Fornax, Sagittarius, and Ursa Minor ([del Pino et al. 2021](#); [Martínez-García et al. 2021, 2022](#)). Thus far, the number of MW satellites for which deriving the internal kinematics is possible is small and hence the number of dSph satellites for which coherent motions are detected. The combination of the lack of gas in dSphs, their distance, and technical limitations make it difficult to study their internal kinematics. However, future measurements of PMs (e.g. *Gaia* Data Release 4) and  $v_{\text{los}}$  may allow us to study the internal kinematics of more satellites of the MW.

The evolution of the internal kinematics of satellites in the subsample of MW dSph analogues reveals a similar behaviour to the other TNG50 dwarf satellites. This can be seen for individual satellites in Fig. 5, where the panels of `subhaloID 554807` and `516783`

correspond to dwarfs in the subsample. The MW dSph analogues had initially higher values of  $|V_T|$  and  $A_{\text{grad}}^{v_z}$  that progressively decreased with time, as we find for the TNG50 satellites. We also observe temporary increases in  $A_{\text{grad}}^{v_z}$  with the pericentre passages, as discussed in Section 3.3. The medians of  $|V_T|$  and  $A_{\text{grad}}^{v_z}$  for all the dwarfs in the subsample at  $z = 0$  are  $1.08 \pm 0.07$  km s<sup>-1</sup> and  $0.91 \pm 0.07$  km s<sup>-1</sup> kpc<sup>-1</sup> respectively. These values can be found in Table 2, where it can be seen that they are similar to the other satellites of TNG50; nonetheless they are lower than the median  $|V_T|$  and  $A_{\text{grad}}^{v_z}$  for the MW dSph satellites ([Martínez-García et al. 2021, 2022](#)). These discrepancies could be explained by the greater uncertainties of  $|V_T|$  and  $A_{\text{grad}}^{v_z}$  in observational studies, since these take into account more sources of error, such as the uncertainties in PMs and  $v_{\text{los}}$  for the bulk and individual stars, among others (for more details see section 2.3 of [Martínez-García et al. 2021](#) and section 2.2 of [Martínez-García et al. 2022](#)). For comparison between observed and simulated MW satellites, we used a Monte Carlo (MC) scheme. In each iteration we randomly choose six MW dSph analogues in order to have a sample whose size is consistent with the number of MW dSphs for which their internal kinematics have been derived ([Martínez-García et al. 2021, 2022](#)). For each of the sampled galaxies, we add to its  $V_T$  a random number from a normal distribution centred on zero and with a dispersion equal to the observational error of  $V_T$  of one of the observed MW dSph satellites of [Martínez-García et al. \(2021\)](#) chosen at random. We then calculate the median value of  $|V_T|$  of the six sampled galaxies. We proceed similarly for  $A_{\text{grad}}^{v_z}$ , adding a random number from a normal distribution centred on zero and a dispersion equal to the observational error of  $A_{\text{grad}}^{v_z}$  of one of the observed MW dSphs of [Martínez-García et al. \(2022\)](#) chosen at random. We then calculate the median value of  $A_{\text{grad}}^{v_z}$  of the six sampled galaxies. This procedure is repeated for  $10^4$  iterations. The distributions of the medians of  $|V_T|$  and  $A_{\text{grad}}^{v_z}$  for all the iterations are shown in Figure 7. We include blue vertical lines and blue-shaded areas that represent the median and the interval between the 0.16 and 0.84 quantiles of all the realizations for  $|V_T|$  ( $2.00^{+1.72}_{-0.90}$  km s<sup>-1</sup>) and  $A_{\text{grad}}^{v_z}$  ( $1.45^{+1.01}_{-0.60}$  km s<sup>-1</sup> kpc<sup>-1</sup>). These values can be found in Table 2. We also include in Figure 7 red vertical lines and red-shaded areas that represent the median and its standard error for  $|V_T|$  and  $A_{\text{grad}}^{v_z}$  for the MW dSph satellites ([Martínez-García et al. 2021, 2022](#)). We observe that the median values of the kinematic features obtained through the MC simulation and the median values for the observed MW dSphs are in good agreement. In the case of  $|V_T|$ , observations and simulations show very similar values. For  $A_{\text{grad}}^{v_z}$ , the results are also similar, but not as close as in the case of  $|V_T|$ . We note that for

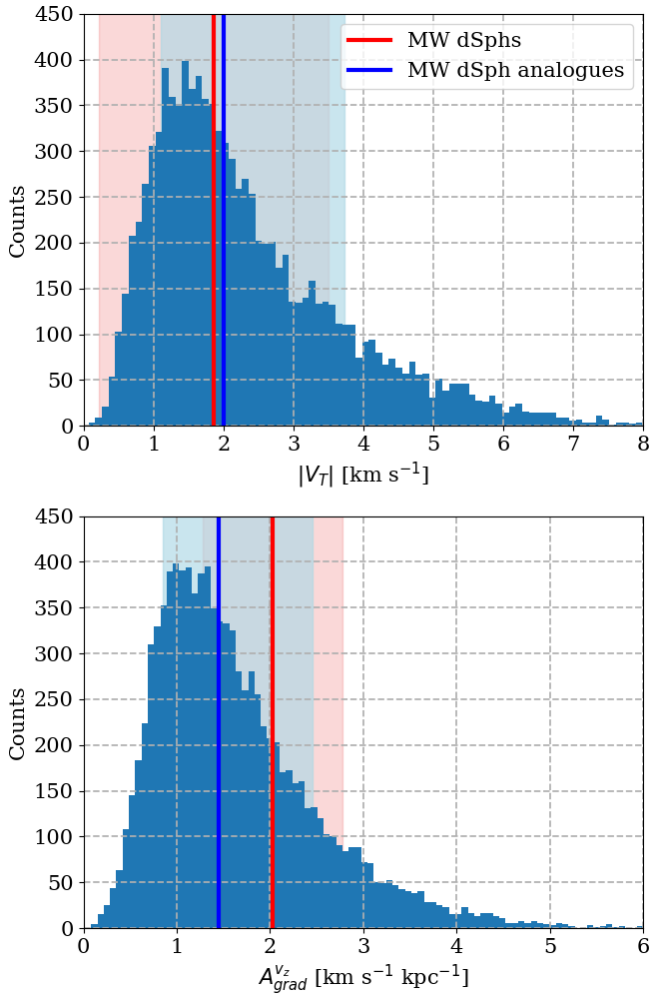


**Figure 7.** Distribution of the median  $|V_T|$  (top panel) and the median  $A_{\text{grad}}^{vz}$  (bottom panel) of the output of the MC simulation of Section 3.5. The blue vertical lines and blue-shaded areas represent the median values and the interval between the 0.16 and 0.84 quantiles of the medians  $|V_T|$  and  $A_{\text{grad}}^{vz}$  for all the realizations. The red vertical lines and the red-shaded areas represent the median and its standard error for  $|V_T|$  and  $A_{\text{grad}}^{vz}$  for the observed MW dSphs (Martínez-García et al. 2021, 2022).

both features the median values for the observed and simulated MW dSphs are consistent at the  $1\sigma$  level.

We analysed the impact of the interaction with the host on the internal kinematics of the MW dSph analogues. In Fig. 8 we show  $f_{\text{peri}}$  and the look-back time for all the MW dSph analogues and all the snapshots of the simulation. We include colour-filled contours of  $|V_T|$  (top panel) and  $A_{\text{grad}}^{vz}$  (bottom panel). Figure 8 is an analogue version of Fig. 6, restricted to the MW dSph analogues. We observe similar trends in both figures, yet for the MW dSph analogues the plot is noisier owing to the lower number of galaxies analysed. The trends in Fig. 8 are sharper compared to Fig. 6 an effect that is likely to be caused by the lower masses of the MW dSph analogues, which makes them more susceptible to the influence of the host. In order to compare these trends with previous observational studies, in Fig. 9 we show  $f_{\text{peri}}$  and  $A_{\text{grad}}^{vz}$  for all the TNG50 satellites and the MW dSph analogues at look-back time  $< 0.5$  Gyr. We cannot restrict the samples strictly to  $z = 0$  because the sample of MW dSph analogues contains a low number of galaxies. Including the last 0.5 Gyr allows

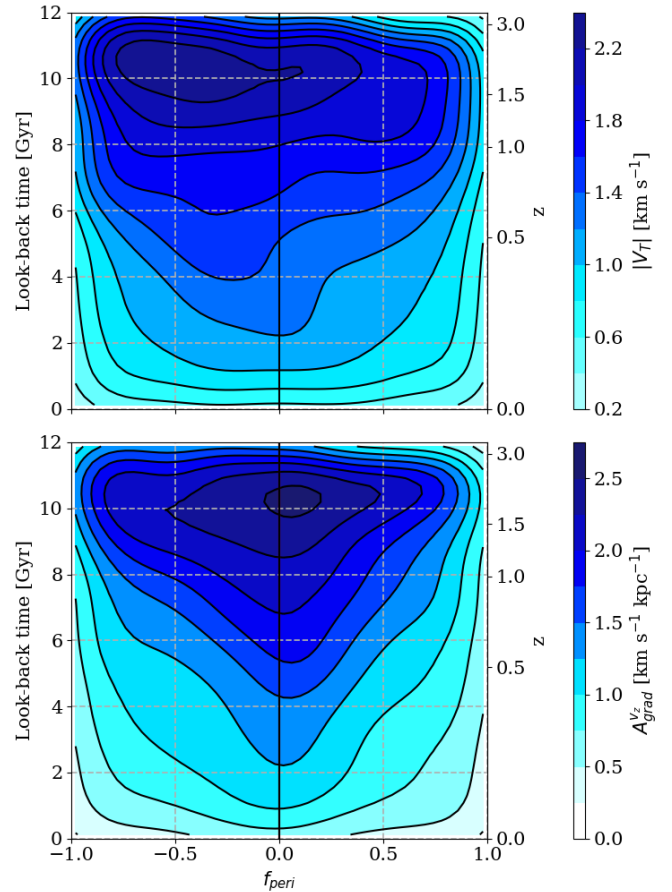


**Figure 8.** Evolution of the internal kinematics of the satellites as a function of the relative position in their orbits for the subsample of MW dSph analogues. Markers coincide with those of Figure 6.

us to increase the statistics while analysing a time span close enough to  $z = 0$ . We used evenly spaced bins along  $f_{\text{peri}}$  and calculated the median  $A_{\text{grad}}^{vz}$  in each bin. Figure 9 represents an analogous version of Fig. 6 and Fig. 8 at  $z \sim 0$ . Both the whole sample of TNG50 satellites and the subsample of MW dSph analogues show a similar behaviour, consistent with Fig. 6 and Fig. 8, and match the reported trend in  $A_{\text{grad}}^{vz}$  for the MW dSph satellites: the amplitude of  $A_{\text{grad}}^{vz}$  tends to increase as the MW dSphs approach their pericentres and  $A_{\text{grad}}^{vz}$  tends to decrease for dwarfs as they head towards their apocentres, the largest values of  $A_{\text{grad}}^{vz}$  being reached in the vicinity of the pericentre (see top panel of fig. 8 of Martínez-García et al. 2022). The fact that simulated and observed galaxies show a similar trend, in which the amplitude of their gradients depends on the position in their orbits suggests that the gradients of the MW dSph satellites are caused by interaction with the MW, and thus the interaction with the host does have an impact on the evolution of the internal kinematics of its satellites.

#### 4 CONCLUSIONS

In this paper, we have studied the internal kinematics of dwarf satellites of the TNG50 simulation. We looked for dwarfs resembling those of the LG, so we explored MW/M31-like hosts and analysed

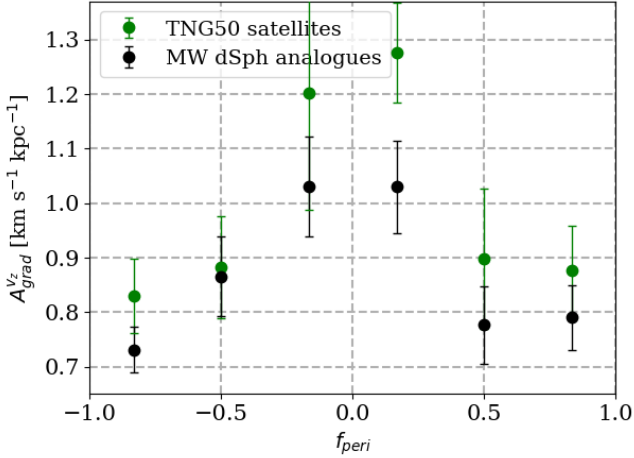


**Figure 9.** Amplitude of the gradients in  $v_z$  of the satellites and their relative position in their orbits during the last 0.5 Gyr. The points represent the median amplitude of the gradients in  $v_z$  of satellites in evenly spaced bins in  $f_{\text{peri}}$ . Green points represent all the selected satellites from TNG50 and black points represent the subsample of MW dSph analogues.

their subhaloes. We selected 1017 dwarf satellites for which we derived their internal kinematics in every snapshot. This allowed us to obtain a historic record of their rotation velocity in the plane of the sky ( $V_T$ ) and the amplitude of their velocity gradients along the line of sight ( $A_{\text{grad}}^{v_z}$ ) corrected for perspective effects.

For the vast majority of the systems, we initially detect rotation in the plane of the sky ( $\sim 65\%$ ) or velocity gradients along the line-of-sight ( $\sim 80\%$ ). These figures were progressively reduced until reaching 45% and 68%, respectively, at  $z = 0$ . Therefore, this suggests that the presence of detectable rotation and gradients along the line of sight in satellites of MW/M31-like hosts is not an uncommon feature at present. We studied possible differences in the evolution of the internal kinematics between dSphs and the other dwarfs (non-dSphs, for simplicity). We observe that the fraction of systems with detected rotation in the plane of the sky and the velocity gradients was originally similar, regardless of the type of dwarf. However, around look-back time  $\sim 10$  Gyr the trends started diverging. We observe a sooner and faster decrease of the ratios for the dSphs. At  $z = 0$ , ratios are lower for dSphs. Additionally, we find that  $|V_T|$  and  $A_{\text{grad}}^{v_z}$  have different distributions at  $z = 0$  for dSphs and non-dSphs. These differences are likely to be due to the different orbital histories of different types of dwarfs. We find that dSphs generally perform their first pericentric passage sooner and experience more passages than non-dSphs, which explains the earlier and more intense decreases in the ratio of rotating systems in the plane of the sky and the ratio of satellites with velocity gradients, and thus the differences in the distributions.

We find that interaction with the host has impacted the evolution of internal kinematics of the satellites. Our analysis of the evolution of  $|V_T|$  in individual satellites reveals that, initially, the satellites had larger values of  $|V_T|$  that were progressively reduced. After first pericentre there is a significant reduction of the rotation in the plane of the sky. The tidal interaction during the passage disrupts the original kinematics, thereby severely reducing the rotation in the plane of the sky. The average rotation velocity is further reduced during successive pericentric passages. Previous studies based on  $N$ -body simulations have found a similar evolution in the rotation velocity of

the dSphs as they interact with their host galaxy (Kazantzidis et al. 2011; Lokas et al. 2010, 2011, 2014, 2015). The evolution of  $A_{\text{grad}}^{v_z}$  is similar, the originally larger values of  $A_{\text{grad}}^{v_z}$  are progressively reduced during pericentric passages. We observe temporary increases of  $A_{\text{grad}}^{v_z}$  during pericentric passages, because the interaction with the host takes place in the direction in which the velocity gradients are measured. Thus, during pericentre the tidal forces tend to induce these velocity gradients in the satellites.

We then analysed the internal kinematics of all the satellites and snapshots simultaneously. We detect a general reduction of  $|V_T|$  and  $A_{\text{grad}}^{v_z}$  with time. We also find that  $|V_T|$  and  $A_{\text{grad}}^{v_z}$  show a different evolution. For  $|V_T|$  we observe a monotonic reduction; however, for  $A_{\text{grad}}^{v_z}$  we observe that during the whole simulation, at any given snapshot  $A_{\text{grad}}^{v_z}$  reaches its highest value close to pericentre. These trends are in agreement with those that we observed in the internal kinematics of individual satellites of TNG50, and are consistent with the different ways in which  $|V_T|$  and  $A_{\text{grad}}^{v_z}$  are impacted by interaction with the host.

We finally restricted our sample of simulated satellites to those that match the properties of the observed MW dSphs, finding a similar evolution of the internal kinematics compared to the entire sample of TNG50 satellites. We observe that the trends in the evolution of  $|V_T|$  and  $A_{\text{grad}}^{v_z}$  are sharper for the MW dSph analogues. This could be because they have lower masses than the other TNG50 satellites and are thus more easily affected by interaction with the host. The trend in  $A_{\text{grad}}^{v_z}$  for MW dSph analogues and TNG50 satellites is similar to that reported for the actual MW dSph satellites, for which  $A_{\text{grad}}^{v_z}$  tends to increase as the satellites move towards their pericentres and is reduced as dwarfs move towards their apocentres, with  $A_{\text{grad}}^{v_z}$  reaching its maximum value in the vicinity of pericentre (Martínez-García et al. 2022). The presence of this trend in both simulated and actual dSph satellites suggests that interaction with the MW is responsible for the observed velocity gradients, and that interaction with the host affects the evolution of the internal kinematics of its satellites.

## ACKNOWLEDGEMENTS

We acknowledge support from the Spanish Agencia Estatal de Investigación del Ministerio de Ciencia e Innovación (AEI-MICINN) under grant ‘Proyectos de I+D+i’ with references AYA2017-89841-P and PID2020-115981GB-I00. AdP acknowledges the financial support from the European Union - NextGenerationEU and the Spanish Ministry of Science and Innovation through the Recovery and Resilience Facility project J-CAVA. The authors also acknowledge all the open-source software involved in this study, especially TOPCAT, Python, and git.

## DATA AVAILABILITY

All the data underlying this article are publicly available. The IllustrisTNG simulations are publicly available and can be found in [www.tng-project.org/data](http://www.tng-project.org/data).

## REFERENCES

Amorisco N. C., Evans N. W., 2012, *MNRAS*, 419, 184

- Battaglia G., Helmi A., Tolstoy E., Irwin M., Hill V., Jablonka P., 2008, *ApJ*, 681, L13
- Battaglia G., Tolstoy E., Helmi A., Irwin M., Parisi P., Hill V., Jablonka P., 2011, *MNRAS*, 411, 1013
- Blumenthal G. R., Faber S. M., Primack J. R., Rees M. J., 1984, *Nature*, 311, 517
- Bullock J. S., Boylan-Kolchin M., 2017, *Annual Review of Astronomy and Astrophysics*, 55, 343
- Cappellari M., Copin Y., 2003, *MNRAS*, 342, 345
- Cardona-Barrero S., Battaglia G., Di Cintio A., Revaz Y., Jablonka P., 2021, *MNRAS*, 505, L100
- Davis M., Efstathiou G., Frenk C. S., White S. D. M., 1985, *ApJ*, 292, 371
- Dekel A., Silk J., 1986, *ApJ*, 303, 39
- del Pino A., Aparicio A., Hidalgo S. L., Lokas E. L., 2017, *MNRAS*, 465, 3708
- del Pino A., Fardal M. A., van der Marel R. P., Lokas E. L., Mateo C., Sohn S. T., 2021, *ApJ*, 908, 244
- Dolag K., Borgani S., Murante G., Springel V., 2009, *MNRAS*, 399, 497
- Ebrova I., Lokas E. L., 2015, *ApJ*, 813, 10
- Engler C., et al., 2021, *MNRAS*, 507, 4211
- Engler C., Pillepich A., Joshi G. D., Pasquali A., Nelson D., Grebel E. K., 2022, *arXiv e-prints*, p. arXiv:2211.00010
- Fabrizio M., et al., 2016, *ApJ*, 830, 126
- Feast M. W., Thackeray A. D., Wesselink A. J., 1961, *MNRAS*, 122, 433
- Gaia Collaboration et al., 2016, *A&A*, 595, A1
- Irwin M., Hatzidimitriou D., 1995, *MNRAS*, 277, 1354
- Joshi G. D., Pillepich A., Nelson D., Zinger E., Marinacci F., Springel V., Vogelsberger M., Hernquist L., 2021, *MNRAS*, 508, 1652
- Kazantzidis S., Lokas E. L., Callegari S., Mayer L., Moustakas L. A., 2011, *ApJ*, 726, 98
- Kirby E. N., Bullock J. S., Boylan-Kolchin M., Kaplinghat M., Cohen J. G., 2014, *MNRAS*, 439, 1015
- Kleyna J., Wilkinson M. I., Evans N. W., Gilmore G., Frayn C., 2002, *MNRAS*, 330, 792
- Klimentowski J., Lokas E. L., Kazantzidis S., Mayer L., Mamon G. A., 2009, *MNRAS*, 397, 2015
- Koch A., Kleyna J. T., Wilkinson M. I., Grebel E. K., Gilmore G. F., Evans N. W., Wyse R. F. G., Harbeck D. R., 2007a, *AJ*, 134, 566
- Koch A., Wilkinson M. I., Kleyna J. T., Gilmore G. F., Grebel E. K., Mackey A. D., Evans N. W., Wyse R. F. G., 2007b, *ApJ*, 657, 241
- Lokas E. L., Kazantzidis S., Majewski S. R., Law D. R., Mayer L., Frinchaboy P. M., 2010, *ApJ*, 725, 1516
- Lokas E. L., Kazantzidis S., Mayer L., 2011, *ApJ*, 739, 46
- Lokas E. L., Athanassoula E., Debattista V. P., Valluri M., Pino A. d., Semechuk M., Gajda G., Kowalczyk K., 2014, *MNRAS*, 445, 1339
- Lokas E. L., Semechuk M., Gajda G., D’Onghia E., 2015, *ApJ*, 810, 100
- Marinacci F., et al., 2018, *MNRAS*, 480, 5113
- Martnez-Garca A. M., del Pino A., Aparicio A., van der Marel R. P., Watkins L. L., 2021, *MNRAS*, 505, 5884
- Martnez-Garca A. M., del Pino A., Aparicio A., 2022, *MNRAS*, 518, 3083
- Mateo M., 1998, *ARA&A*, 36, 435
- Mayer L., 2010, *Advances in Astronomy*, 2010, 278434
- McConnachie A. W., 2012, *AJ*, 144
- McConnachie A. W., Venn K. A., 2020, *AJ*, 160, 124
- Munoz R. R., et al., 2006, *ApJ*, 649, 201
- Munoz R. R., et al., 2005, *ApJ*, 631, L137
- Naiman J. P., et al., 2018, *MNRAS*, 477, 1206
- Navarro J. F., Frenk C. S., White S. D. M., 1995, *MNRAS*, 275, 720
- Nelson D., et al., 2018, *MNRAS*, 475, 624
- Nelson D., et al., 2019a, *Computational Astrophysics and Cosmology*, 6, 2
- Nelson D., et al., 2019b, *MNRAS*, 490, 3234
- Pace A. B., et al., 2020, *MNRAS*, 495, 3022
- Patel E., Besla G., Sohn S. T., 2017, *MNRAS*, 464, 3825
- Patel E., Besla G., Mandel K., Sohn S. T., 2018, *ApJ*, 857, 78
- Pillepich A., et al., 2018a, *MNRAS*, 473, 4077
- Pillepich A., et al., 2018b, *MNRAS*, 475, 648
- Pillepich A., et al., 2019, *MNRAS*, 490, 3196
- Planck Collaboration et al., 2016, *A&A*, 594, A13
- Putman M. E., Zheng Y., Price-Whelan A. M., Grcevich J., Johnson A. C., Tollerud E., Peek J. E. G., 2021, *ApJ*, 913, 53
- Rodrguez-Gomez V., et al., 2015, *MNRAS*, 449, 49
- Sales L. V., et al., 2015, *MNRAS*, 447, L6
- Springel V., 2010, *MNRAS*, 401, 791
- Springel V., White S. D. M., Tormen G., Kauffmann G., 2001, *MNRAS*, 328, 726
- Springel V., et al., 2018, *MNRAS*, 475, 676
- van der Marel R. P., Cioni M.-R. L., 2001, *AJ*, 122, 1807
- van der Marel R. P., Alves D. R., Hardy E., Suntzeff N. B., 2002, *AJ*, 124, 2639
- Walker M. G., Mateo M., Olszewski E. W., 2009, *AJ*, 137, 3100
- Weinberger R., et al., 2017, *MNRAS*, 465, 3291
- Weisz D. R., Dolphin A. E., Skillman E. D., Holtzman J., Gilbert K. M., Dalcanton J. J., Williams B. F., 2014, *ApJ*, 789, 147
- Wheeler C., et al., 2017, *MNRAS*, 465, 2420
- White S. D. M., Rees M. J., 1978, *MNRAS*, 183, 341
- Wilkinson M. I., Kleyna J. T., Evans N. W., Gilmore G. F., Irwin M. J., Grebel E. K., 2004, *ApJ*, 611, L21
- Zhu L., van de Ven G., Watkins L. L., Posti L., 2016, *MNRAS*, 463, 1117

This paper has been typeset from a  $\text{\TeX}/\text{\LaTeX}$  file prepared by the author.